DOI: 10.13009/EUCASS2019-519

DOI: ADD DOINUMBER HERE

Reynolds number influence on the hysteresis behavior of a dual-bell nozzle

Alexander Barklage[⋆†], *Simon Loosen*[‡], *Wolfgang Schröder*[‡] *and Rolf Radespiel*[⋆]
[⋆] *Institute of Fluid Mechanics, TU Braunschweig, Hermann-Blenk Str. 37, 38108 Braunschweig*
[‡] *Institute of Aerodynamics, RWTH Aachen University, Wüllnerstraße 5a, 52062 Aachen*
a.barklage@tu-bs.de
[†]Corresponding author

Abstract

This paper considers the influence of Reynolds number on the transition behavior of a dual-bell nozzle with special regard to hysteresis. For this purpose, Reynolds averaged Navier-Stokes (RANS) as well as large-eddy simulations (LES) are performed for a dual-bell nozzle applying a time dependent chamber pressure. Besides turbulent flow conditions, also laminar flows are assumed, i.e., the solutions are sought without considering any turbulence model. The comparison of numerical and experimental results shows a consistent shift of the transition to lower values for turbulent flow.

1. Introduction

The reduction in operational costs for space launchers is becoming more important due to an increasing number of commercial launches and competitors in the market. The performance of the propulsion system and thus the nozzle has a strong influence on the operational costs which creates the need for improving the system. Conventional nozzle types used in today's launchers are bell-shaped with a fixed geometry. These nozzle types have the drawback that they only perform optimally at a specific altitude. At all other altitudes, they produce performance losses due to the non adapted nozzle. This can be avoided by the use of altitude compensating nozzles. The dual-bell nozzle is promising in this respect due to its low system complexity. This nozzle concept was proposed by Foster and Cowles[5] in 1949. It features a one-step altitude compensation that is realized by a contour inflection which divides the nozzle into two bell-shaped contours. At low altitude (sea-level mode), the nozzle flow separates at this contour inflection and since the separation is symmetrical only little side loads are generated. At a higher altitude, the nozzle switches to a full flowing operation mode (altitude mode) due to the lower ambient pressure. Figure 1 shows a sketch of the two operating modes.

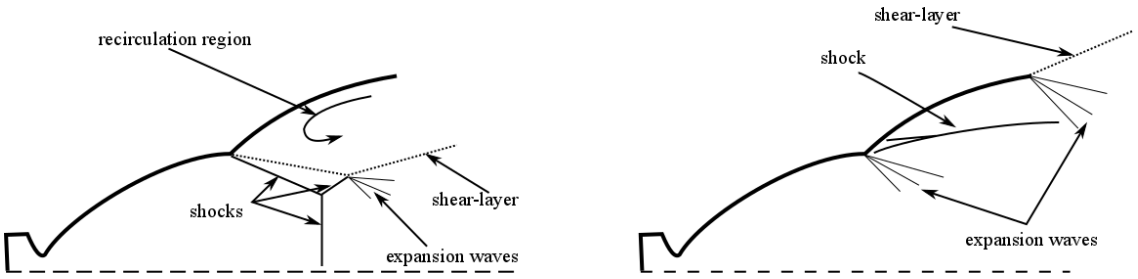

Figure 1: Schematic overview on the two operation modes of a dual-bell nozzle: sea-level mode (left) and altitude mode (right)

Horn and Fisher[15] performed first experimental measurements on dual-bell nozzles. They observed performance losses of the dual-bell nozzle. In sea-level mode a so called aspiration drag occurs due to the fact that the pressure in the separated nozzle flow is lower than the ambient pressure. In altitude mode losses are induced by the non-optimized nozzle contour of the second bell. Additional losses emerge because the transition to altitude mode occurs at lower chamber pressures than an optimal transition. Despite these performance losses, the dual-bell nozzle still delivers more thrust than conventional nozzles. Stark et. al[26] computed the payload gain for Ariane 5 using a dual-bell nozzle to about 480 kg. Quite a number of further studies concerning the performance of dual-bell nozzles have been carried out

DOI: 10.13009/EUCASS2019-519

in the literature.[10,11,13,17]
The largest uncertainty in the design of a dual-bell nozzle is related to the transition from sea-level to altitude mode where high side-loads can be generated, as shown by Genin et. al[12] and by Verma et.al.[31] The transition is therefore desired to be fast and a retransition to sea-level mode should be avoided. Especially, an alternating switching between the two operating modes should be avoided. This phenomenon is known as flip flop effect and the dual-bell nozzle by design features a hysteresis behavior that suppresses the occurrence of the flip-flop effect. Experiments on the hysteresis behavior of dual-bell nozzles have been carried out by Genin et. al.[11] and they detected a strong influence of the design of the nozzle on the hysteresis gap. Schneider et. al.[23] performed numerical studies by means of Reynolds averaged Navier-Stokes equations on the hysteresis behavior. The results agreed well with experimental data and proved RANS simulations capable of describing the hysteresis behavior. Verma et.al.[32] investigated the effect of pressure fluctuations on the transition behavior of a dual-bell nozzle. They showed the transition to be sensitive to pressure fluctuations of the back flow leading to a flip-flop mode when the fluctuations exceed 20 % of the back pressure. Numerical simulations with a fluctuating ambient pressure were performed by Perigo et. al.[21] The dual-bell nozzle is exposed to a fluctuating back pressure by the wake flow of the launcher main body. This buffeting phenomenon has already been extensively studied in the literature, e.g. in.[6,7] Recent studies on a generic space launcher equipped with a dual bell nozzle[2] revealed a flip flop mode when a supersonic outer flow is present. This flip flop mode might be triggered or intensified by laminar nozzle flow conditions.
For this purpose, this paper discusses the Reynolds number influence on the hysteresis behavior of a sub-scale dual-bell nozzle by numerical simulations and experimental measurements. Numerical simulations cover Reynolds averaged Navier-Stokes as well as large-eddy simulations carried out for laminar and turbulent flow conditions. Measurements are performed for different ambient pressures to determine the Reynolds number influence on the transition.
This paper is structured as follows. In the first part, the nozzle geometry and the experimental and numerical setup are described. The laminar and turbulent conditions are then compared and discussed. Conclusions follow in the last section and an outlook is given.

2. Nozzle geometry

In this paper a sub-scale dual-bell nozzle is considered which is mounted to a wind tunnel model of a generic space launcher configuration. Figure 2 gives an overview on the geometry of the wind tunnel model. The dual-bell nozzle consists two nozzle segments separated by a contour inflection. The first segment is designed as a conventional truncated ideal contour (TIC) nozzle with a design Mach number of 3.5. This contour is truncated so that a Mach number of 2.54 is achieved at its end. The second part is designed as a constant pressure extension. This guarantees a fast transition to altitude mode, as discussed in.[14] The angle at the wall inflection is 9.6° and the angle at the exit of the second nozzle is 4.7°.

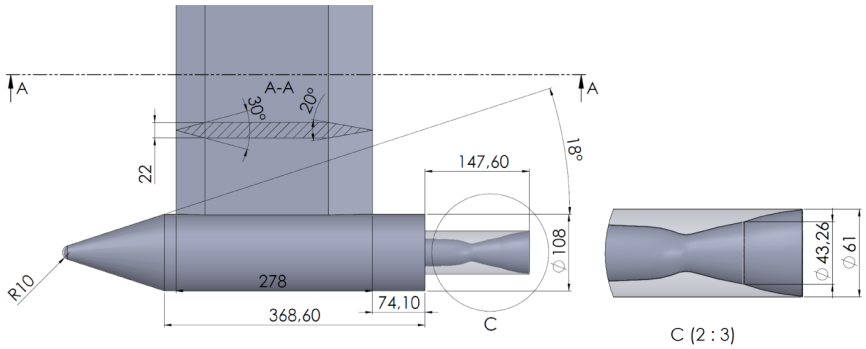

Figure 2: Geometry of wind tunnel model equipped with the investigated dual-bell nozzle

The transition from sea-level to altitude mode is predicted for a nozzle pressure ratio of $NPR_{tr} = p_0/p_\infty = 12.6$. This value was calculated using:[20]

$$NPR_{tr} = \frac{1}{M_e}\left(1 + \frac{\gamma - 1}{2} M_e^2\right)^{\frac{\gamma}{\gamma-1}} \tag{1}$$

where M_e is the Mach number in the nozzle extension and γ is the heat capacity ratio of the propulsive gas. This criterion is based on the Stark separation criterion[27] which was proposed for conventional bell type nozzles. The Stark separation criterion is an empirical criterion that is based on experimental data for turbulent nozzle flow.

DOI: 10.13009/EUCASS2019-519

The numerical simulations neglect the launcher main body since an outer flow is not considered in this study. Therefore, the numerical simulations use a simplified geometry containing the inner nozzle contour and the nozzle fairing. The URANS simulations are restricted to an axisymmetric representation of the nozzle.

3. Experimental and numerical setup

3.1 Experimental setup

Experimental measurements were conducted in the short-duration facility Ludwieg tube Braunschweig (HLB) with a test section diameter of 0.5 m. The facility is capable of simulating hypersonic flow conditions with a freestream Mach number of $Ma_\infty = 6$ and supersonic flow conditions with a freestream Mach number of $Ma_\infty = 3$. The measurement time of the HLB is about 60 ms. A more detailed description of the wind tunnel can be found in Estorf et al.[8] and Wu et al.[34,35] A jet flow can be introduced using the jet simulation facility, TSA[1] , that is also based on the Ludwieg tube working principle. The TSA is sketched in figure 3 on the left hand side. The storage tube has a length of 32 m and a diameter of 18.9 mm leading to a measurement time of 100 ms. The jet facility uses a tandem nozzle design which is housed in the wind tunnel model and consists of a first nozzle, a settling chamber and the dual-bell nozzle. The settling chamber contains perforated plates to homogenize the flow. The first nozzle is exchangeable, wherefore the chamber total pressure can be varied in a wide range. The total pressure in the settling chamber is related to the ratio of the throat diameters by:[16]

$$\frac{p_{0,1}}{p_{0,2}} = \left(\frac{D_2}{D_1}\right)^2 \tag{2}$$

where $p_{0,1}$ is the total pressure in the storage tube, $p_{0,2}$ is the total pressure in the settling chamber, D_1 is the throat diameter of the first nozzle, and D_2 is the throat diameter of the dual-bell nozzle. The ratio of throat diameters is $D_2/D_1 = 6.33$ for settling chamber pressures up to approximately 1 bar and $D_2/D_1 = 2.3$ for pressures ranging from 1 to 4 bars. The settling chamber pressure is measured by two pressure sensors separated by 120° at the end of the settling chamber. A detailed description of the TSA can be found in Stephan et al.[30]

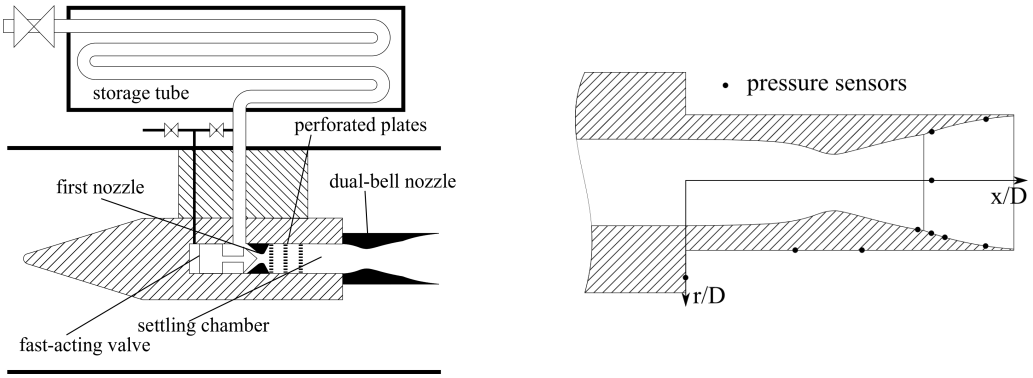

Figure 3: Sketch of the TSA (left) and instrumentation of the wind tunnel model (right)

The wind tunnel model is equipped with 12 time-resolving pressure sensors flush mounted to the surface. Seven of these sensors are located on the nozzle wall, whereas the remaining 5 sensors are located at the base and on the nozzle fairing. On the nozzle wall, the pressure is measured at axial positions measured from the base of $x/D = 0.96,\ 1.02,\ 1.08$ and 1.25 where D is the main body diameter. The most upstream position of $x/D = 0.96$ is located in the first bell and the other 3 positions are located in the second bell. At an axial position of $x/D = 1.02$, the pressure is measured at three different angular positions of $\phi = 180°,\ 90°$, and 0° measured from the model support. At an axial position of $x/D = 1.25$, the pressure is measured at angular positions of $\phi = 180°$ and 0°. The pressure data is recorded by a Spectrum M2i.4652 recorder at a frequency of 3 Mhz.

[1]German abbreviation for '**T**reibstrahl **S**imulations **A**nlage'

DOI: 10.13009/EUCASS2019-519

3.2 Numerical setup

3.2.1 Reynolds averaged Navier-Stokes computations

Unsteady Reynolds averaged Navier-Stokes computations were performed using the DLR TAU code.[24] The code solves the compressible Navier-Stokes equations on structured and unstructured grids in a conservative finite-volume formulation. In this study, the two-dimensional, axisymmetric equations are solved. The Spalart-Allmaras turbulence model[25] closes the RANS equations. Euler terms are discretized by an AUSMDV upwind scheme[33] and inviscid terms are discretized by a central scheme with second-order accuracy. A backward Euler scheme with dual-time stepping was used for temporal integration. Different time step sizes of $1 \cdot 10^{-5} s$, $5 \cdot 10^{-6} s$ and $1 \cdot 10^{-6} s$ were tested and a time step size of $5 \cdot 10^{-6} s$ showed to be most promising in terms of accuracy and computational time.

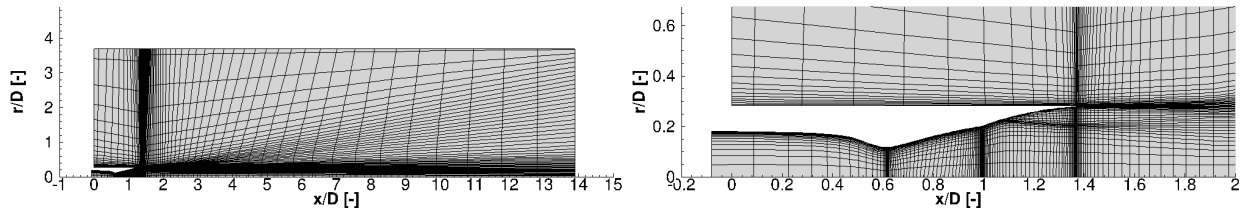

Figure 4: Computational grid of the URANS calculations. Every 6th grid point is shown

The computational domain extends in the axial direction from $x/D = 0$ to $x/D = 13.9$ measured from the base. It extends in the radial direction from $r/D = 0$ to $r/D = 3.7$ with D being the main body diameter of the launcher model. Total conditions in terms of total pressure and density are prescribed at the nozzle inflow. The nozzle wall and fairing are modeled as isothermal viscous wall. Farfield conditions are prescribed on all other boundaries. Axisymmetric boundaries are set in the circumferential direction. A gradient of zero for the flow variables represents a symmetrical axis at $r/D = 0$. The grid is two-dimensional and structured and counts 190,000 cells. The y^+ value is below 0.8 on the nozzle wall for all cases.

3.2.2 Zonal RANS-LES

The zonal RANS/LES solver developed at the Institute of Aerodynamics of RWTH Aachen University was used to analyze various transonic[28] and supersonic[29] rocket flows. The three-dimensional compressible Navier-Stokes equations are solved based on a conservative finite-volume scheme. Euler terms are discretized by a mixed centered upwind AUSM scheme[18] of second order accuracy. A second order central scheme with second order accuracy approximates the inviscid terms. Temporal integration is performed using an explicit 5-stage Runge-Kutta method with second order accuracy. The monotone integrated LES (MILES) models the sub-grid scales of the LES by numerical dissipation.[3] A detailed description of the LES solver can be found in Meinke et al.[19] The LES solution can be coupled to a RANS solution via a Reformulated Synthetic Turbulence Generation (RSTG) method according to Roidl et al.[22] A one-equation turbulence model of Fares and Schröder[9] closes the RANS equations. This zonal RANS LES approach saves computational time since the LES is only conducted in regions where flow separation occurs.
The computations were performed in two steps without a direct coupling between RANS and LES. In a first step the RANS equations were solved with time dependent nozzle conditions. A data base for the LES was then created for discrete time steps with a separation of $\Delta t = 0.1 t_{ref}$ with $t_{ref} = (tD)/u_{in}$ where u_{in} is the velocity at the nozzle inlet. This data base was then used to calculate the boundary conditions at the inlet of the LES domain by linear interpolation in time. This saves a lot of computational time compared to a fully coupled computation since the LES does not have to use the time step of the RANS which is about one order of magnitude lower. A coupled RANS and LES computation is not necessary since the coupling from LES to RANS is very weak due to the hyperbolic character of the conservation equations in this region.

Figure 5 shows the RANS and LES domain for the dual-bell nozzle. Both, the RANS and LES grid are fully structured. The RANS domain contains the nozzle flowfield and extends in axial direction from $x/D = 0.08$ to the nozzle exit at $x/D = 1.367$. The RANS domain describes an axisymmetric representation of the nozzle with an extent in circumferential direction of 9°. At the inflow total conditions are prescribed and at the outflow a supersonic outflow is specified. The nozzle wall is modeled as an adiabatic wall. The y^+-value at the wall is always below 1 and the grid counts about one million cells.
The RANS/LES interface is located upstream of the contour inflection at a position of $x/D = 0.867$ in order to provide a fully established boundary layer at the contour inflection. The LES domain extends in the axial direction from

DOI: 10.13009/EUCASS2019-519

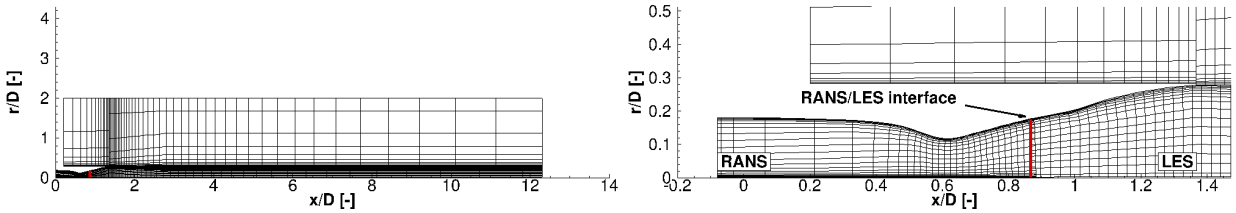

Figure 5: Computational grid for zonal RANS/LES computation for the low Reynolds number case. Every 10th grid point is shown.

$x/D = 0.2$ to $x/D = 12.3$. In the circumferential direction the grid spans over $\phi = 360°$. The radial extent of the LES grid is $r/D = 2$. The nozzle wall and fairing are modeled as adiabatic viscous wall. At the nozzle inflow the boundary conditions are determined by the RANS solution. The remaining boundaries satisfy farfield conditions using a characteristic approach. In the region of the RANS/LES interface and on the nozzle wall, the average grid resolution of the LES is $\Delta x/y^+ = 30$, $\Delta r/y^+ = 2$ and $\Delta\phi/y^+ = 20$. The number of cells for the LES grid is for the low Reynolds number case 77 million and for the high Reynolds number case 277 million. This mesh resolution corresponds to typical mesh requirements for wall-bounded flows.[4] The CFL number for the RANS and LES is 1.5.

3.3 Test cases

The working gas is for all investigations air at a temperature of 295 K. Experiments were conducted with steady nozzle inlet conditions. Numerical simulations were carried out with steady nozzle inlet conditions as well as with a varying pressure at the nozzle inlet to investigate the hysteresis behavior. The pressure was varied linearly with a slope of $\Delta NPR/\Delta t = 1.26$. This value was chosen according to Schneider et al.[23] which showed a good comparison with measurements. In the experiments, no outer flow is present while in the simulations an outer flow with a Mach number of $Ma_\infty = 0.1$ was prescribed due to enhanced numerical stability of the compressible solver.
Different nozzle Reynolds number regimes were simulated by increasing the nozzle pressure range and the ambient pressure. Two Reynolds number regimes were investigated numerically. These will be referred to as 'low Reynolds number case' and 'high Reynolds number case'. For the low Reynolds number case, the outer pressure is $p_\infty = 4100\ Pa$ and for the high Reynolds number case, it is $p_\infty = 16400\ Pa$.

4. Results

4.1 Quasi-steady Results

The results of LES and RANS calculations for steady nozzle inlet conditions are compared to experimental results in this chapter. Flow separation is the dominating flow phenomenon during the transition process and can be characterized by the pressure distribution inside the nozzle. Figure 6 shows a comparison of numerical and experimental results at high Reynolds number and low Reynolds number conditions in sea-level mode. For the high Reynolds number case the nozzle Reynolds number is $Re^* = 6.18 \cdot 10^5$ and for the low Reynolds number case it is $Re^* = 1.55 \cdot 10^5$. The nozzle Reynolds number is calculated by $Re^* = (\rho^* u^* d^*)/\mu^*$ where the star denotes nozzle throat conditions. A laminar flow is expected for the low Reynolds number case wherefore RANS simulations without turbulence modeling are performed additionally for this case. Experimental values for the mean pressure are averaged over a time period of $\Delta t = 40\ t_{ref}$. Mean pressures of the LES solution are calculated by averaging in the circumferential direction by $\Delta\phi = 360°$ and in time by $\Delta t = 1.5\ t_{ref}$.
The RANS as well as the LES solution show a good agreement with the experimental data for the high Reynolds number case. The flow clearly separates at the contour inflection which is located at $x/D = 0.99$ in the LES solution and the experiment. The separation can be identified in the mean pressure distribution by an increase of pressure in the second bell above the altitude mode value which is $p/p_0 = 0.028$. In the RANS solution, the nozzle flow separates in the second bell at approximately $x/D = 1.01$. This behavior was not observed in the experiments where no separation in the second bell occurred for both values of NPR. The LES solution therefore shows more convincing results. In the low Reynolds number case, the separation occurs earlier than for the high Reynolds number case since the pressure increases downstream of the contour inflection in the experiment. The LES solution matches very well with the experimental data whereas the turbulent RANS solution deviates from the experimental data. The turbulent RANS solution reveals a separation in the second bell at approximately $x/D = 1.15$ which is not present in the experiments. The laminar solution shows a much better comparison with the experimental and LES results. The nozzle flow also

DOI: 10.13009/EUCASS2019-519

separates at the contour inflection for the laminar solution. Hence, it can be assumed that in the low Reynolds number case the nozzle flow is laminar. To get a closer look into the boundary layer state of the LES simulation the Q-criterion is considered.

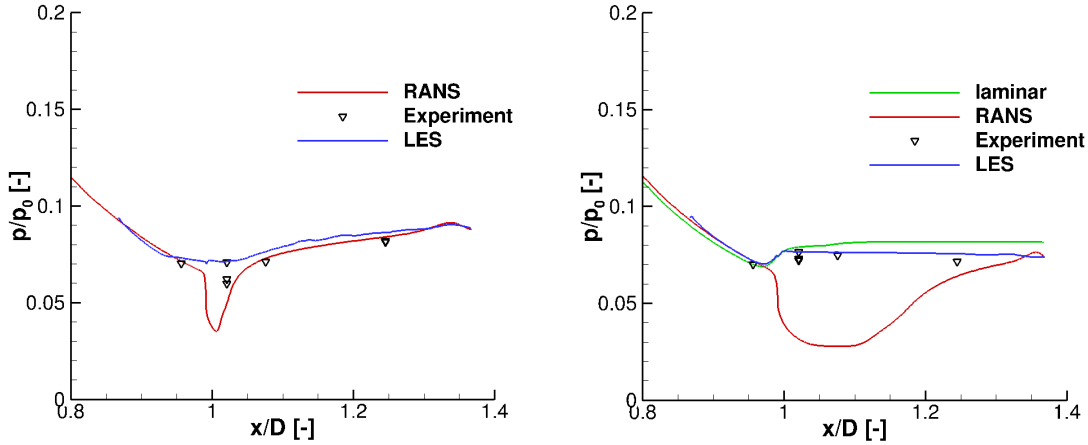

Figure 6: Pressure distribution on the nozzle wall for $NPR = 10$ at high Reynolds number condition (left) and for $NPR = 12$ at low Reynolds number condition (right).

The Q-criterion contours for an $NPR = 20$ are shown in Fig. 7 for both Reynolds number regimes. This corresponds to altitude mode since the NPR is above the predicted transition value of $NPR_{trans} = 12.6$ For the high Reynolds number conditions turbulent structures in the boundary layer are clearly visible and are present from the LES inlet plane until the nozzle exit. For the low Reynolds number case turbulent structures are visible at the LES inlet which slowly decay and no turbulent structures are present in the initial part of the separated shear layer. The shear layer seems to be laminar to a position of approximately $x/D = 1.25$ where it becomes unstable. Note that the high Reynolds number case shows an attached nozzle flow in the whole second bell whereas at the low Reynolds number the flow separates in the second bell. This is caused by the fact that a laminar boundary layer separates at lower pressure gradients compared to a turbulent boundary layer. The transition behavior for laminar and turbulent flow therefore differs strongly as will be shown in chapter 4.2.

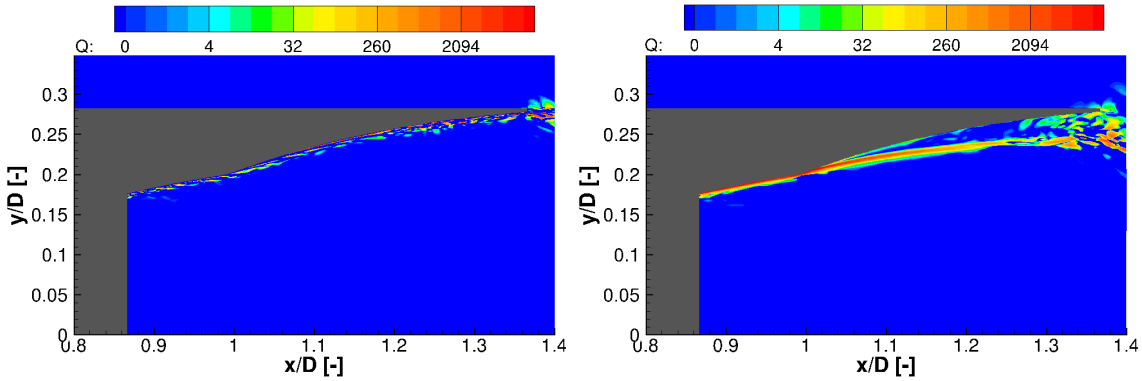

Figure 7: Q-criterion contours for $NPR = 20$ at high Reynolds number condition (left) and low Reynolds number condition (right).

4.2 Hysteresis calculations

Hysteresis calculations were carried out for the low Reynolds number case where laminar flow is expected and for the high Reynolds number case where turbulent flow is expected. For the laminar case URANS calculations are carried out with and without a turbulence model.
To characterize the transition and retransition process, the position of flow separation inside the nozzle is evaluated.

DOI: 10.13009/EUCASS2019-519

Note that the transition process refers to the switch the from sea-level to the altitude mode and the retransition process refers to the switch from the altitude mode to the sea-level mode. The separation position inside the nozzle is determined by the condition that the friction coefficient c_f equals zero at this position. Figure 8 left depicts the separation position for the LES results. The separation position in this figure is averaged in the circumferential direction. The transition process for laminar and turbulent conditions is obviously very different. The NPR-value for which transition and retransition occur is much higher for the laminar case then for the turbulent case. This is again related to the fact that a laminar boundary separates at lower pressure gradients than a turbulent boundary layer. Thus, for the laminar case the transition occurs at higher chamber pressures and at a corresponding higher NPR-value than for the turbulent case. The laminar solution features a phenomenon known as nozzle sneak transition, where no sudden transition occurs but instead the separation position is fixed for a certain NPR range in the second bell. This phenomenon was also measured at lower Reynolds numbers compared to this case.[1] The turbulent case does not reveal this behavior and transition and retransition occur in a small NPR range. The transition occurs in a smaller NPR range than the retransition. The turbulent case also features a much more pronounced hysteresis gap than the laminar solution where transition and retransition almost coincide at a approximately $NPR = 25$. Thus, the dual-bell nozzle is more stable against a possible flip-flop mode for turbulent nozzle flow conditions.
To characterize the side loads that are generated during transition and retransition the root mean square of the separation position is used. The root-mean square value of the separation position is calculated by:

$$x_{sep,rms} = \frac{1}{n-1}\left(\sum_{i=1}^{n} x_{i,sep}^2 - \frac{1}{n}\left(\sum_{i=1}^{n} x_{i,sep}\right)^2\right) \tag{3}$$

where n is the number of grid points in the circumferential direction and $x_{i,sep}$ is the separation position at a certain circumferential position. This value is shown in Fig. 8 right. The laminar solution exhibits very little side loads when the nozzle is in sea-level or altitude mode. During transition and retransition the side loads increase. The side loads during transition are higher than during retransition. The peak value occurs at the NPR-value where the slope $d(x_{sep})/d(NPR)$ exhibits its maximum value. The turbulent solution shows higher peak values of $x_{sep,rms}$ compared to the laminar solution. Analogously to the laminar solution the side loads during transition are higher than during retransition. Side loads almost vanish when the nozzle is in sea-level mode and the separation is very symmetrical in the circumferential direction. In altitude mode, side loads are increased compared to the side loads in sea-level mode.

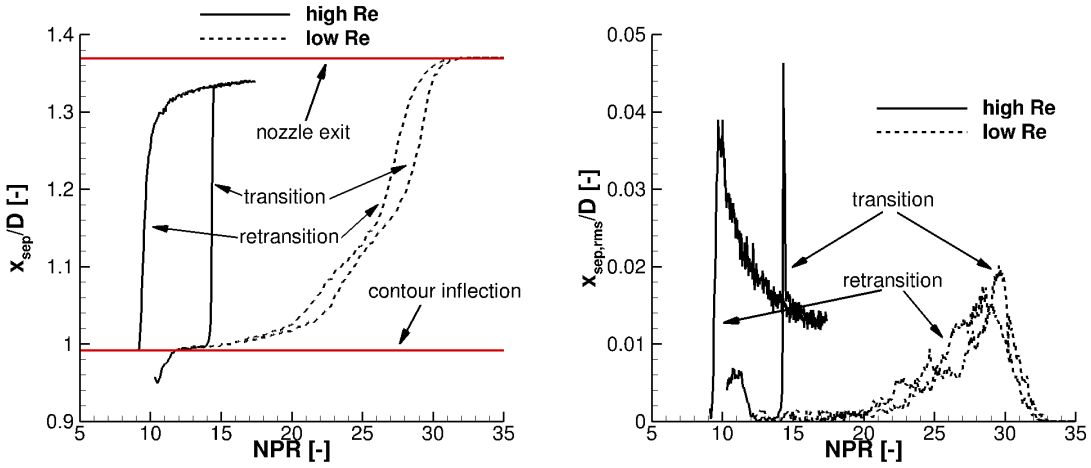

Figure 8: Position of flow separation (left) and root-mean square value of the separation position in circumferential direction (right) for the LES solution.

Figure 9 right shows the results of the URANS hysteresis calculations. All three simulations started at around $NPR = 10$ and the simulations with a turbulence model ended at $NPR = 25$ whereas the laminar calculation ended at $NPR = 35$. At $NPR = 10$ the laminar solution reveals a separation of the nozzle flow upstream of the contour inflection while in the turbulent cases the separation is fixed at the contour inflection. The transition to altitude mode occurs at a much higher NPR-value for the laminar case compared to the turbulent cases. All URANS cases feature a sneak transition that is most pronounced for the laminar case. Comparing the turbulent solutions for low and high Reynolds number case, the sneak transition is more pronounced for lower Reynolds numbers. With increasing Reynolds number both the transition and retransition are shifted to lower NPR-values.

DOI: 10.13009/EUCASS2019-519

The hysteresis gap characterizes the stability of the nozzle against pressure fluctuations of the chamber pressure or the ambient pressure and is defined by:

$$H = \frac{NPR_{tran} - NPR_{retran}}{NPR_{tran}} \tag{4}$$

where H is the hysteresis gap, NPR_{tran} and NPR_{retran} are the NPR-values for transition and retransition. The values for NPR_{tran} and NPR_{retran} were defined at the location where the slope of $d(x_{sep})/d(NPR)$ features a maximum. Table 1 gives an overview on the hysteresis gap for all numerical simulations. The URANS results predict a larger hysteresis gap for higher Reynolds numbers what is in alignment with the LES results. However, the absolute value for the hysteresis gap differs since the LES predicts a much larger hysteresis gap for the high Reynolds number case compared to the URANS solution. Additionally, the NPR-values for transition and retransition for the low Reynolds number LES solution are increased compared to the corresponding turbulent URANS solution and are comparable with the laminar URANS case, again revealing this case to be laminar. The laminar result features a larger hysteresis gap compared to the turbulent URANS solutions, in contrast to the LES results which showed a larger hysteresis gap for the turbulent case.

Table 1: Transition / retransition NPR and hysteresis gap for the numerical results

	LES low Re	**LES high Re**	**laminar solution low Re**	**URANS low Re**	**URANS high Re**
NPR_{tran}	29.12	14.33	28.29	11.78	11.06
NPR_{retran}	27.38	9.37	23.22	10.81	9.75
H	0.060	0.346	0.179	0.082	0.118

A comparison with experimental results is given in figure 9 right. Note that it is not possible to predict the hysteresis gap in the experiments since the jet simulation facility does not allow to simulate a varying chamber pressure. The experimentally measured transition NPR therefore corresponds to a quasi-steady value. This value was determined by a subsequent stepwise increase of the chamber pressure until transition to altitude mode occurred. As the step size was approximately $\Delta NPR = 0.3$, the error in NPR_{tr} is of the same order. The experimental measurements indicate that transition to altitude mode takes place at increased NPR-values for decreasing Reynolds numbers, for low Reynolds numbers. Whereas for the Reynolds number range of $Re^* = 6.68 \cdot 10^5 - 1.3 \cdot 10^6$ no considerable change in transition NPR can be observed. Comparing the experimental and numerical results, there is a good agreement for the high Reynolds number case whereas for the low Reynolds number the results differ. The experimentally measured transition NPR at the low Reynolds number case lies above the turbulent URANS solution but below the value of the laminar solution and the LES solution. This indicates that the boundary layer in the experiment is neither laminar or turbulent but in a transitional state. The turbulent URANS simulation shows almost no change in transition NPR for the low and high Reynolds number case what is also true in the experiment for $Re^* > 6.68 \cdot 10^5$. This NPR-value is in good alignment with the value of $NPR_{tr} = 12.6$ using the transition criterion shown in equation 1 which assumes turbulent separation. It can therefore be concluded that for Reynolds numbers above approximately $Re^* = 6.68 \cdot 10^5$ the nozzle flow is turbulent and for lower Reynolds numbers the nozzle flow is laminar or in a transitional state.

5. Conclusions

LES and URANS simulations were performed on a sub-scale dual-bell nozzle at different nozzle Reynolds number regimes to investigate the hysteresis behaviour. The numerical results are validated by experimental data in terms of pressure distribution and transition NPR.

For the pressure distribution at sea level conditions, the LES shows a good agreement with experimental data for both Reynolds number cases. The turbulent URANS solution delivers good results for the high Reynolds number case but for the low Reynolds number case the laminar solution is more accurate revealing the low Reynolds number case to be laminar. The LES solution for the low Reynolds number case corresponds to a laminar solution since no turbulent structures can be observed by evaluating the Q-criterion. The hysteresis calculations for the laminar case feature a sneak transition in the LES and URANS results. In contrast, in the turbulent LES solutions the transition occurs much faster whereas the transition in the URANS solution occurs always in a broader NPR range than in the LES solution. The hysteresis gap for the turbulent case is increased compared to the laminar case in the LES solution leading to a more stable operation of the nozzle for turbulent conditions. The URANS computations, however, showed a larger hysteresis gap for the laminar solution. Side loads during transition and retransition were characterised by evaluating the symmetry of flow separation by means of $x_{sep,rms}$. The side loads for the turbulent case are increased compared to the laminar case during the transition and retransition phase. The side loads during transition showed to

DOI: 10.13009/EUCASS2019-519

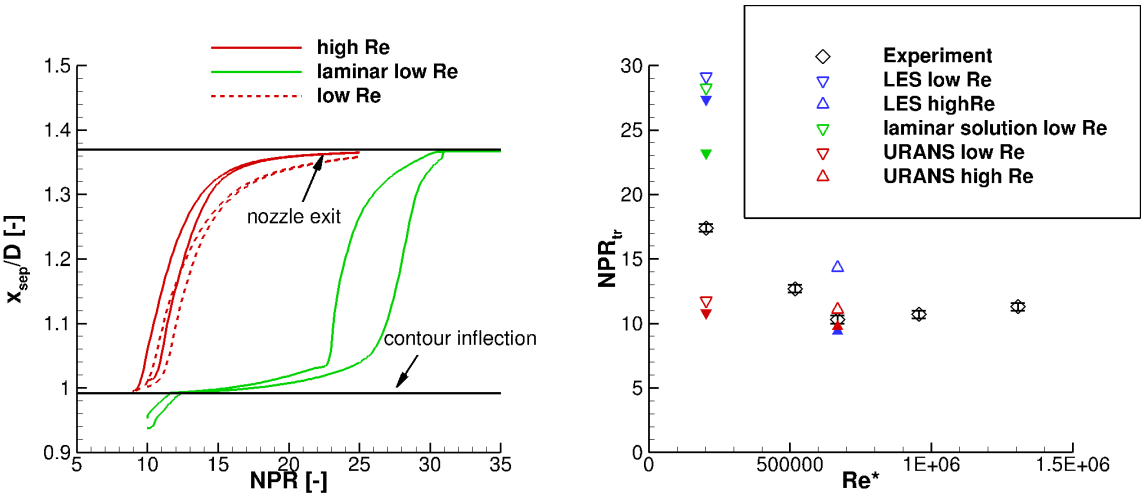

Figure 9: Position of flow separation for URANS calculation (left) and *NPR* value for transition as a function of nozzle Reynolds number Re^* of the experimental measurements and the numerical simulations (right), open symbols stand for transition and filled symbols for retransition

be higher than during retransition. The transition and retransition NPR of the numerical simulations were compared to experimental results. The numerical results agreed well with experimental data for the high Reynolds number case. For the low Reynolds number case the numerical simulations predict a higher NPR-value for transition and retransition compared to the experiment. The numerical simulations and the measurements revealed a shift of the transition NPR to higher values for the low Reynolds number case. The boundary layer state in the experiments is assumed to be in a transitional state at the low Reynolds number since the transition NPR is above the turbulent URANS solution but below the laminar solution. It was also observed that the transition NPR in the experiments does not change considerably for $Re^* > 6.68 \cdot 10^5$ and corresponds to the value of the turbulent LES-simulation. Therefore, a turbulent nozzle flow can be assumed for these Reynolds numbers.
Future work will consider the influence of an outer flow on the transition behaviour of the nozzle since experiments showed a strong influence of the outer flow. This will include a variation of the afterbody geometry of the launcher model which has a strong influence on the back pressure that determines the nozzle transition. The influence of the nozzle design on the hysteresis bahaviour will also be investigated. For this purpose, future investigations focus on a dual-bell nozzle with a positive pressure gradient extension which is known to increase the hysteresis gap.

6. Acknowledgments

Financial support has been provided by the German Research Foundation (Deutsche Forschungsgemeinschaft - DFG) in the framework of the Sonderforschungsbereich Transregio 40. Computational resources have been provided by the High Performance Computing Center Stuttgart(HLRS) and by the North-German Supercomputing Alliance (HLRN).

References

[1] A. Barklage and R. Radespiel. Influence of the boundary layer state on the transition of a dual-bell nozzle. Deutsche Gesellschaft für Luft- und Raumfahrt - Lilienthal-Oberth e.V., 2019. urn:nbn:de:101:1-201901251351199534981 2.

[2] A. Barklage, R. Radespiel, and C. Génin. Afterbody jet interaction of a dual-bell nozzle in supersonic flow. In *AIAA Propulsion and Energy Forum*. American Institute of Aeronautics and Astronautics, July 2018. AIAA Paper 2018-4468.

[3] J. Boris, F. Grinstein, E. Oran, and R. Kolbe. New insights into large eddy simulation. *Fluid dynamics research*, 10(4-6):199–228, 1992.

[4] H. Choi and P. Moin. Grid-point requirements for large eddy simulation: Chapman s estimates revisited. *Physics of fluids*, 24(1):011702, 2012.

DOI: 10.13009/EUCASS2019-519

[5] F. B. Cowles and C. R. Foster. Experimental study of gas-flow separation in overexpanded exhaust nozzles for rocket motors. *JPL Progress report*, pages 4–103, 1949.

[6] S. Deck and P. Thorigny. Unsteadiness of an axisymmetric separating-reattaching flow: Numerical investigation. *Physics of Fluids*, 19:1–20, 2007.

[7] D. Deprés and P. Reijasse. Analysis of unsteadiness in afterbody transonic flows. *AIAA journal*, 42(12):2541–2550, 2004.

[8] M. Estorf, T. Wolf, and R. Radespiel. Experimental and numerical investigations on the operation of the hypersonic ludwieg tube braunschweig. In *Fifth European Symposium on Aerothermodynamics for Space Vehicles*, volume 563, page 579, 2005.

[9] E. Fares and W. Schröder. A general one-equation turbulence model for free shear and wall-bounded flows. *Flow, Turbulence and Combustion*, 73(3-4):187–215, 2005.

[10] M. Frey and G. Hagemann. Critical assessment of dual-bell nozzles. *Journal of Propulsion and Power*, 15(1):137–143, 1999.

[11] C. Génin and R. Stark. Flow transition in dual bell nozzles. *Shock Waves*, 19(3):265–270, 2009.

[12] C. Génin and R. Stark. Side loads in subscale dual bell nozzles. *Journal of Propulsion and Power*, 27(4):828–837, 2011.

[13] G. Hagemann, H. Immich, T. V. Nguyen, and G. E. Dumnov. Advanced rocket nozzles. *Journal of Propulsion and Power*, 14(5):620–634, 1998.

[14] G. Hagemann, M. Terhardt, and D. Haeseler. Experimental and analytical design verification of the dual-bell concept. *Journal of Propulsion and Power*, 18(1):116–122, 2002.

[15] M. Horn and S. Fisher. Dual-bell altitude compensating nozzles. Technical report, NASA, 1994.

[16] J. D. Anderson Jr. *Modern Compressible Flow With Historical Perspective*. Mc Graw-Hill, New York, 3 edition, 2002.

[17] T. Kimura, K. Niu, K. Yonezawa, Y. Tsujimoto, and K. Ishizaka. Experimental and analytical study for design of dual-bell nozzles. In *45th AIAA Joint Propulsion Conference*, 2009. AIAA Paper 2009-5149.

[18] M.-S. Liou and C. J. Steffen. A new flux splitting scheme. *Journal of Computational physics*, 107(1):23–39, 1993.

[19] M. Meinke, W. Schröder, E. Krause, and T. Rister. A comparison of second-and sixth-order methods for large-eddy simulations. *Computers & Fluids*, 31(4-7):695–718, 2002.

[20] C. Nürnberger-Génin and R. Stark. Experimental study on flow transition in dual bell nozzles. *Journal of Propulsion and Power*, 26(3):497–502, 2010.

[21] D. Perigo, R. Schwane, and H. Wong. A numerical comparison of the flow in conventional and dual bell nozzles in the presence of an unsteady external pressure environment. In *39th AIAA/ASME/SAE/ASEE Joint Propulsion Conference and Exhibit*. American Institute of Aeronautics and Astronautics, 2003. AIAA Paper 2003-4731.

[22] B. Roidl, M. Meinke, and W. Schröder. A reformulated synthetic turbulence generation method for a zonal rans–les method and its application to zero-pressure gradient boundary layers. *International Journal of Heat and Fluid Flow*, 44:28–40, 2013.

[23] D. Schneider and C. Génin. Numerical investigation of flow transition behavior in cold flow dual-bell rocket nozzles. *Journal of Propulsion and Power*, 32(5):1212–1219, 2016.

[24] D. Schwamborn, T. Gerhold, and R. Heinrich. The DLR TAU-Code: Recent Applications in Research and Industry. In *Proceedings of the European Conference on Computational Fluid Dynamics (ECCOMAS)*, 2006.

[25] P. R. Spalart and S. R. Allmaras. A one-equation turbulence model for aerodynamic flows. *30th Aerospace Sciences Meeting and Exhibit*, (AIAA Paper 92-0439), 1992.

DOI: 10.13009/EUCASS2019-519

[26] R. Stark, C. Génin, D. Schneider, and C. Fromm. Ariane 5 performance optimization using dual-bell nozzle extension. *Journal of Spacecraft and Rockets*, 53(4):743–750, 2016.

[27] R. Stark and B. Wagner. Experimental study of boundary layer separation in truncated ideal contour nozzles. *Shock Waves*, 19(3):185–191, 2009.

[28] V. Statnikov, M. Meinke, and W. Schröder. Reduced-order analysis of buffet flow of space launchers. *Journal of Fluid Mechanics*, 815:1–25, 2017.

[29] V. Statnikov, T. Sayadi, M. Meinke, P. Schmid, and W. Schröder. Analysis of pressure perturbation sources on a generic space launcher after-body in supersonic flow using zonal turbulence modeling and dynamic mode decomposition. *Physics of Fluids*, 27(1):016103, 2015.

[30] S. Stephan, J. Wu, and R. Radespiel. Propulsive jet influence on generic launcher base flow. *CEAS Space Journal*, 7:453–473, 2015.

[31] S. B. Verma, C. Stark, R. énin, and O. Haidn. Cold-gas experiments to study the flow separation characteristics of a dual-bell nozzle during its transition modes. *Shock Waves*, 20:191–203, 2010.

[32] S.B. Verma, R. Stark, and O. Haidn. Effect of ambient pressure fluctuations on dual-bell transition behavior. *Journal of Propulsion and Power*, 30(5):1192–1198, 2014.

[33] Y. Wada and M.-S. Liou. A flux splitting scheme with high-resolution and robustness for discontinuities. In *32nd Aerospace Sciences Meeting and Exhibit*, 1994. AIAA Paper 94-0083.

[34] J. Wu and R. Radespiel. Tandem nozzle supersonic wind tunnel design. *International Journal of Engineering Systems Modelling and Simulation 47*, 5(1-3):8–18, 2013.

[35] J. Wu and R. Radespiel. Experimental investigation of a newly designed supersonic wind tunnel. In *Progress in Flight Physics*, volume 7, pages 123–144. EDP Sciences, 2015.